

1 **Impact of aerosol hygroscopic growth on retrieving aerosol extinction coefficient** 2 **profiles from elastic-backscatter lidar signals**

3 Gang Zhao¹, Chunsheng Zhao¹, Ye Kuang¹, Jiangchuan Tao¹, Wangshu Tan¹, Yuxuan Bian², Jing Li¹,
4 Chengcai Li¹

5 1 Department of Atmospheric and Oceanic Sciences, School of Physics, Peking University, Beijing,
6 China

7 2 State Key Laboratory of Severe Weather, Chinese Academy of Meteorological Sciences, Beijing,
8 100081, China

9 *Correspondence to: Chunsheng Zhao (zcs@pku.edu.cn)*

10 **Abstract**

11 Light detection and ranging (lidar) measurements have been widely used to profile ambient
12 aerosol extinction coefficient (σ_{ext}). The particle extinction-to-backscatter ratio (lidar ratio, LR), which
13 strongly depends on the aerosol dry particle number size distribution (PNSD) and aerosol
14 hygroscopicity, is introduced to retrieve the σ_{ext} profile from elastic-backscatter lidar signals.
15 Conventionally, a constant column-integrated LR that is estimated from aerosol optical depth is used
16 by the retrieving algorithms. In this paper, the influences of aerosol PNSD, aerosol hygroscopic growth
17 and relative humidity (RH) profiles on the variation of LR are investigated based on the datasets from
18 field measurements in the North China Plain (NCP). Results show that LR has an enhancement factor
19 of 2.2 when RH reaches 92%. Simulation results indicate that both the magnitude and vertical
20 structures of the σ_{ext} profiles by using column-related LR method are significantly biased from the
21 original σ_{ext} profile. The relative bias, which is mainly influenced by RH and PNSD, can reach up to 40%
22 when RH at the top of the mixed layer is above 90%. A new algorithm for retrieving σ_{ext} profiles and a
23 new scheme of LR enhancement factor by RH in the NCP are proposed in this study. The relative bias
24 between the σ_{ext} profile retrieved with this new algorithm and the ideal true value is reduced to below
25 13%.

26 **1. Introduction**

27 Atmospheric aerosols can directly scatter and absorb solar radiation, thus exerting significant
28 impacts on the atmospheric environment and climate change. Vertical distributions of aerosol particles
29 are crucial for studying the roles of atmospheric aerosols in the radiation balance of the

30 Earth-Atmosphere system (Kuang et al., 2016), air pollution transportation (Gasteiger et al., 2017) and
31 boundary layer process. However, there remain many problems while determining the spatial and
32 temporal distributions of aerosols because of their highly variable properties (Anderson and Anderson,
33 2003; Andreae and Crutzen, 1997) and complex sources. As a result, our knowledge about the vertical
34 distributions of aerosols is still very limited.

35 Light detection and ranging (lidar) instruments are useful remote sensing tools to monitor profiles
36 of aerosol optical properties. This kind of instrument involves a pulsed laser beam, which can be used
37 to detect the back-scatter signals from aerosols and air molecules in the atmosphere (Klett, 1981).
38 Elastic-backscatter lidar is one of the most frequently used instruments (He et al., 2006; Pietruczuk and
39 Podgórski, 2009). However, there are some limitations when deriving aerosol extinction coefficient
40 (σ_{ext}) and aerosol backscattering coefficient (β_{sca}) from elastic-backscatter lidar signals. Many efforts
41 have been carried out to retrieve the σ_{ext} profiles from lidar signals (Klett, 1981, 1985). Particle
42 extinction-to-backscatter ratio, which is usually termed as the lidar ratio (LR), is required when
43 retrieving σ_{ext} profiles (Fernald, 1984; Fernald et al., 1972). LR can be derived directly using Raman
44 lidar (Pappalardo et al., 2004b) and high spectral resolution lidar (She et al., 1992; Shipley et al., 1983;
45 Sroga et al., 1983) measurements. Raman lidar has low signal to noise ratios (SNR) during the day,
46 which may lead to significant bias and uncertainties in retrieving lidar signals. High spectral resolution
47 lidar have high technique requirement and expensive cost. Ansmann et al. (2002) demonstrated that the
48 profile of LR could be retrieved from Raman lidar and this LR profile can be used to retrieve σ_{ext}
49 profiles from high SNR elastic-backscattering lidar data. However, there exist many cases when
50 elastic-backscatter lidar is used without concurrently measured LR profile.

51 Sun-photometer, radiometer and elastic-backscatter lidar data are usually used simultaneously to
52 retrieve σ_{ext} profiles (Chaikovsky et al., 2016; He et al., 2006). In these studies, σ_{ext} profiles could be
53 retrieved from elastic-backscatter lidar signals by using a constant column-related LR, which is
54 constrained by measurements of aerosol optical depth (AOD) from sun-photometer. However, many
55 factors such as aerosol particle number size distribution (PNSD), aerosol refractive index, aerosol
56 hygroscopicity and ambient relative humidity (RH), have large influences on LR. It is found that the
57 ratio of σ_{ext} and β_{sca} grows linearly but slowly as RH increases when RH is lower than 80%
58 (Ackermann, 1998; Anderson et al., 2000; Ferrare et al., 2001). Further research found that LR is
59 likely to change significantly due to the substantial variation of RH in the mixed layer (Ferrare et al.,

1998). Small errors from the initial conditions may lead to large bias of retrieved σ_{ext} profiles (Sušnik et al., 2014). It is likely that using a constant LR profile instead of variable LR profile to retrieve elastic-backscatter lidar data may result in significant bias of retrieved σ_{ext} profiles. The sounding profiles show that RH is highly variable, frequently exceeding 80% in the mixed layer in the NCP (Kuang et al., 2016) which is one of the most polluted areas around the world (Ma et al., 2011; Xu et al., 2011). Accordingly, it is interesting to know by how much σ_{ext} profiles retrieved from elastic-backscatter lidar signals will deviate if a constant column-related LR profile is used in the NCP. Few studies have been performed to assess the bias of using a constant LR profile. This work comprehensively studies the possible bias by employing a large dataset of field measurements.

To account for aerosol hygroscopic growth, κ -Köhler theory (Petters and Kreidenweis, 2007) is widely used, in which the chemical composition-dependent variables are merged into a single parameter κ . The κ -Köhler equation is expressed as

$$\frac{RH}{100} = \frac{GF^3 - 1}{GF^3 - (1 - \kappa)} \cdot \exp\left(\frac{4\sigma_s/\alpha M_{\text{water}}}{R \cdot T \cdot D_d \cdot g_f \cdot \rho_w}\right), \quad (1)$$

where D_d is the aerosol dry diameter, GF is the aerosol growth factor, which is defined as the ratio of the aerosol diameter under the given RH and dry conditions (D_{RH}/D_d), T is the temperature, $\sigma_{s/a}$ is the surface tension of the solution, M_{water} is the molecular weight of water, R is the universal gas constant and ρ_w is the density of water.

This article is structured in the following way. Section 2 shows all of the data used in this study. Section 3 gives the methodology of this research. Mie theory (Bohren and Huffman, 2007) and κ -Köhler theory (Petters and Kreidenweis, 2007) are used to study the influences of aerosol hygroscopic growth on LR. By calculating the LR at different RH, it is found that the RH-related LR profiles are significantly different from the constant LR profile as shown in fig. 1(b). We simulate the bias of the retrieved σ_{ext} profiles by using the AOD related constant LR profiles in three steps. Firstly, the vertical distributions of the aerosol are parameterized and the corresponding aerosol σ_{ext} and β_{sca} profiles are calculated in section 3.2. Secondly, we calculate the theoretical signals received by the elastic-backscatter lidar in section 3.3 by using the σ_{ext} and β_{sca} profiles of the first step. Finally, we retrieve the σ_{ext} profiles from the lidar signals of section 3.3 by using the column related lidar ratio profiles, in which the method is detailed in section 3.4.1. The retrieved σ_{ext} profiles are compared with the parameterized σ_{ext} profiles. In section 3.4.2, we propose a new method of retrieving the σ_{ext} profiles,

89 which can account for the variations of LR with RH. Results and discussions are shown in section 4.
90 Section 4.2 shows the bias of retrieved σ_{ext} profiles by using a column-related LR profile method.
91 Section 4.2.1 gives the possible bias of the retrieved σ_{ext} profiles and section 4.2.2 shows the sensitivity
92 of the bias under different AOD, different aerosol PNSD, different RH profiles and different aerosol
93 hygroscopicity conditions. In section 4.4, real-time field measurements from a micro-pulsed lidar
94 (MPL) are used to validate the feasibility of our new proposed method. The conclusions of this
95 research are summarized in section 5.

96 **2. Data**

97 **2.1 Datasets of aerosol properties**

98 During the periods of Haze in China (HaChi) campaign, the physical and chemical properties of
99 aerosol particles were measured at the Wuqing meteorological station ($39^{\circ} 23' \text{N}$, $117^{\circ} 0' \text{E}$, 7.4 m
100 a.s.l.). Wuqing is located between two megacities (Beijing and Tianjin) of NCP, and can represent the
101 pollution conditions of the NCP (Xu et al., 2011).

102 This study uses the measured datasets of PNSD, black carbon (BC) mass concentrations (Ma et al.,
103 2012) and aerosol hygroscopicity (Chen et al., 2014; Liu et al., 2014) during the field campaign. The
104 sampled aerosol particles are selected to have an aerodynamic diameter of less than 10 μm by an
105 impactor at the initial inlet. These particles are carefully dried to below 40% RH and then led to the
106 corresponding instruments. The aerosol PNSDs with particle diameter in the range from 10nm to 10 μm
107 are measured by jointly using a differential mobility particle sizer (TDMPS, Leibniz Institute for
108 Tropospheric Research, Germany; Birmili et al., 1999) and an aerodynamic particle sizer (APS, TSI
109 Inc., model 3321) with a temporal resolution of 5 min. The BC mass concentrations are measured by a
110 multi-angle absorption photometer (MAAP model 5012, Thermo, Inc., Waltham, MA USA). The
111 aerosol hygroscopicity is measured by using the humidity tandem differential mobility analyzer
112 (HTDMA), which measures the aerosol GF as a function of RH at different diameter. The aerosol
113 hygroscopicity parameter κ can be directly derived from measurements of the HTDMA by applying
114 formula (1).

115 **2.2 RH profiles**

116 The intensive GTS1 observation (Bian et al., 2011) at the meteorological bureau of Beijing ($39^{\circ} 48'$
117 N , $116^{\circ} 28' \text{E}$) were carried out from July to September 2008. With a resolution of 10m in the vertical
118 direction, the radiosonde data include profiles of temperature, pressure and RH. During the intensive

119 observation period, balloon soundings were performed four times a day.

120 Water vapor mixing ratio is almost constant in the mixed layer due to extensive turbulent mixing,
121 and decreases rapidly above the mixed layer. RH profiles that exhibit well-mixed vertical structures
122 were selected and studied. RH profiles are classified into four typical groups based on the maximum
123 RH ranges: 60%-70%, 70%-80%, 80%-90% and 90%-95% (Kuang et al., 2016). These four kinds of
124 typical well-mixed RH profiles are labeled as P60-70, P70-80, P80-90 and P90-95 respectively. These
125 four kinds of RH profiles, which are shown in fig. 1(a), are used to conduct the sensitivity studies in
126 this article.

127 **2.3 MPL signals**

128 A single wavelength polarization diversity elastic lidar system is installed on the roof of the
129 physics building in Peking University. This instrument is a MPL manufactured by Sigma Space, using
130 a Nd: YVO4 532nm pulsed DC10H-532SS laser source, with a pulse duration of 10.3ns, energy of
131 6-8uJ and a repetition of 2500Hz. It collects elastically backscattered signals from the atmosphere by
132 separately detecting its parallel and cross polarization components with respect to the polarization of
133 laser. We also used the concurrently measured AOD data from the AERONET BEIJING_PKU station,
134 which is located at the same place as the Lidar.

135 **3. Methodology**

136 **3.1 Influences of aerosol hygroscopic growth on LR**

137 **3.1.1 Calculate the LR values under different RH conditions**

138 In this paper, the Mie model (Bohren and Huffman, 2007) is used to study the influence of RH on
139 LR. When running the Mie model, aerosol PNSD, aerosol complex refractive index, black carbon
140 mixing state and black carbon mass concentrations are essential. The results of the Mie model contain
141 the information about σ_{ext} and β_{sca} , which can be used to calculate the LR directly, with $\text{LR} = \frac{\sigma_{\text{ext}}}{\beta_{\text{sca}}}$.

142 When exposed to ambient, the aerosols grow. To account for this, we use the size-resolved
143 hygroscopicity parameter κ , which is derived from the measurements of the HTDMA (Chen et al.,
144 2012; Liu et al., 2011). This size-resolved κ is shown in fig. S1. Mean distribution of the size-resolved
145 κ during the Hachi Campaign is used. With this, the aerosol GF for different D_a and RH can be
146 calculated by applying formula (1).

147 Mixing states of BC come from the measurements during the Hachi Campaign. In previous work,

148 BC mixing states during the Hachi campaign were presented as both core-shell mixed and externally
 149 mixed (Ma et al., 2012). Ma et al. (2012) provides the ratio of BC mass concentration under externally
 150 mixed state, M_{ext_BC} , to total BC mass concentration, M_{BC} , as follows:

$$151 \quad r_{ext_BC} = \frac{M_{ext_BC}}{M_{BC}} \quad (2).$$

152 The mean value of $r_{ext_BC}=0.51$ (Ma et al., 2012) is used as a representation of the mixing state in this
 153 study. The size-resolved distribution of BC mass concentration is the same as that used by Ma et al
 154 (2012a).

155 The refractive index (\tilde{m}), accounting for the water content in the particle, is derived as a volume
 156 mixture between the dry aerosol and water (Wex et al., 2002):

$$157 \quad \tilde{m} = f_{v,dry} \tilde{m}_{aero,dry} + (1 - f_{v,dry}) \tilde{m}_{water} \quad (3).$$

158 $f_{v,dry}$ is the ratio of the dry aerosol volume to total aerosol volume at given RH condition; $\tilde{m}_{aero,dry}$ is
 159 the refractive index of dry ambient aerosols and \tilde{m}_{water} is the refractive index of water. The
 160 refractive indices of BC, non-light-absorbing aerosols and water, which are used in this study, are
 161 $1.8+0.54i$ (Kuang et al., 2015), $1.53+10^{-7}i$ (Wex et al., 2002) and $1.33+10^{-7}$ respectively.

162 To sum up, we can calculate the LR of a PNSD under the given RH condition by using the Mie
 163 scattering model. For a dry aerosol PNSD, the corresponding aerosol PNSD at a given RH can be
 164 calculated by applying the mean distribution of size-resolved κ and formula (1). Aerosol refractive
 165 index can be determined from formula (3), too. With this information, LR can be calculated. For each
 166 aerosol PNSD, we change the RH from 40% to 95% to calculate the LR values at different RH. Finally,
 167 the LR values of different measured aerosol PNSD at different RH are calculated by using the same
 168 method.

169 **3.1.2 Parameterizing the variation of LR with RH**

170 When the LR values under different RH are statistically studied, we find that the LR can be
 171 enhanced when the RH increases, which will be discussed in detail in section 4.1.1 and fig 2.

172 The LR enhancement factor is introduced to describe the influence of aerosol hygroscopic growth
 173 on LR at different RH. It is defined as the ratio of LR at a given RH to LR at the condition of $RH < 40\%$.
 174 We give the statistical mean relationships between the LR enhancement factor and RH. The LR
 175 enhancement factor can account for the increase of LR with RH and the parameterized LR
 176 enhancement factor is further used in our proposed method to retrieve the σ_{ext} profiles.

177 **3.2 LR profiles and σ_{ext} profiles**

178 Liu et al. (2009) studied vertical profiles of aerosol total number concentration (Na) with aircraft
179 measurements, and derived a parameterized vertical distribution. In this scheme, Na is constant in the
180 mixed layer, with a transition layer where it linearly decreases and an exponential decrease of Na
181 above the transition layer. The same parameterized scheme proposed by Liu et al. (2009) is adopted by
182 this study. Both the study of Liu et al. (2009) and Ferrero et al. (2010) manifest that the dry aerosol
183 PNSD in the mixed layer varies little. The shape of the dry aerosol PNSD is assumed constant with
184 height, which means that aerosol PNSD at different heights divided by Na give the same normalized
185 PNSD.

186 As for the BC vertical distribution, Ferrero et al. (2011) and Ran et al. (2016) demonstrate that BC
187 mass concentration in the mixed layer remains relatively constant and decreases sharply above the
188 mixed layer. According to this, the parameterization scheme of BC vertical distribution is assumed to
189 be the same as that of aerosol. The shape of the size-resolved BC mass concentration distribution is
190 also assumed to be the same as that at the surface.

191 LR profiles and σ_{ext} profiles can be calculated by Mie theory under these assumptions. Details of
192 computing σ_{ext} profiles can be found at Kuang et al. (2015). The calculated LR profiles and σ_{ext}
193 profiles are used in the following study to provide the theoretical elastic-backscatter signals.

194 **3.3 Simulated elastic-backscatter lidar signals**

195 The intensity of signals received by elastic-backscatter lidar depends on optical properties of
196 objects and the distance between scattering objects and receiving system. It can be typically described
197 by the following formula:

$$198 \quad P(R) = C \times P_0 \times \frac{\beta(R)}{R^2} \times e^{\int_0^R -2 \times \sigma(r) \times dr} \quad (4).$$

199 In formula (4), P_0 is the intensity of the laser pulse, R is the spatial distance between scattering
200 objects and the receiving system, C is a correction factor determined by the status of
201 elastic-backscatter lidar machine itself, $\beta(R)$ refers to the sum of aerosol backscattering coefficient
202 (β_{sca}) and air molecule backscattering coefficient ($\beta_{\text{sca,mole}}$) at distance R , $\sigma(R)$ denotes the sum of σ_{ext}
203 and air molecule's extinction coefficient ($\sigma_{\text{ext,mole}}$). $\beta_{\text{sca,mole}}$ and $\sigma_{\text{ext,mole}}$ can be calculated by using
204 Rayleigh scattering theory when the temperature and pressure are available.

205 In this study, we can theoretically get the intensities of elastic-backscatter lidar signals and the

206 AOD from each given σ_{ext} and β_{sca} profiles with the assumption that C is equal to one. Retrieving
207 elastic-backscatter lidar signals can result in exactly the same σ_{ext} profile as the original one when the
208 profile of LR is available. However, using a constant column-related LR profile to retrieve
209 elastic-backscatter lidar signals will cause the retrieved σ_{ext} profile deviate from the initial σ_{ext} profile.

210 **3.4 Retrieving σ_{ext} profiles from elastic-backscatter lidar signals**

211 **3.4.1 Retrieving σ_{ext} profiles by using constant column-related LR profile method**

212 Traditionally, the AOD from sun-photometer and the elastic-backscatter lidar signals are
213 combined to retrieve the σ_{ext} profiles. Additional information is needed to get the mathematical results
214 of formula (4) because there are two unknown parameters (β_{sca} and σ_{ext}). The commonly used method
215 of solving this formula is to assume a constant value of column-related LR and then the profiles of σ_{ext}
216 and β_{ext} can be retrieved (Fernald, 1984; Klett, 1985). Different values of column-related LR can lead
217 to different σ_{ext} profiles and different AOD. A constant column-related LR can be constrained if the
218 sun photometer is concurrently measuring the AOD (He et al., 2006; Pietruczuk and Podgorski, 2009).
219 Thus, the σ_{ext} profile can be retrieved by using the column-related constant LR profile.

220 **3.4.2 Retrieving σ_{ext} profiles accounting for aerosol hygroscopic growth**

221 A new method of retrieving σ_{ext} profiles from elastic-backscatter lidar signals is proposed, in
222 which the variation of LR with RH can be taken into consideration. This new method requires the
223 measured elastic-backscatter lidar signals, measured AOD data and RH profiles.

224 A schematic diagram of this method is shown in Fig.2. A parameterized LR profile is used to
225 retrieve σ_{ext} profiles instead of an AOD-constrained constant LR profile. Firstly, the LR enhancement
226 factors are statistically studied and parameterized under different polluted conditions. The results of
227 the mean parameterized LR enhancement factor, which is detailed in section 4.1.1, are used in this
228 study. The LR profile can be calculated by using the RH profile, a LR for dry aerosol and the
229 equations of LR enhancement factor. The σ_{ext} profile can be retrieved with a combination of LR profile
230 and formula (4). The dry state LR value can be constrained by comparing the integrated AOD value of
231 the retrieved σ_{ext} profile and concurrently measured AOD value. The LR profile is determined and the
232 σ_{ext} profile can be retrieved with the constrained dry state LR.

233 **4. Results and Discussion**

234 **4.1 LR properties**

235 **4.1.1 Variation of LR with RH**

236 During the field campaign of Hachi, 3540 different aerosol PNSDs were measured. These aerosol
 237 PNSDs can be used as a good representative dataset for the continental aerosol. LR is calculated by
 238 using different aerosol PNSD and RH values between 30% and 95%.

239 Relationships between the dry state LR and concurrently measured σ_{ext} (sum of the aerosol
 240 scattering and absorption) are shown in Fig. 2(a). It shows that LR can vary across a wide range from
 241 30 sr to 90 sr, which is consistent with the literature values of continental aerosols (Ansmann et al.,
 242 2001; Pappalardo et al., 2004a). This also indicates that calculating the LR by using Mie theory is
 243 feasible. Fig. 2(b) gives the probability distribution function of the LR. Most of the LR lies in the
 244 range between 45~65 sr.

245 By calculating the LR values under different RH, we find that the LR tends to increase with RH.
 246 Relationships between the LR enhancement factor and RH are given in Fig. 2(c). The LR enhancement
 247 factor has a mean value lower than 1.2 when the RH is lower than 70%. LR increases linearly with RH
 248 when RH is lower than 80%. However, LR can be enhanced by a factor of 2.2 when the RH reaches 92%
 249 with mean hygroscopicity of aerosol.

250 Mean values of LR enhancement factor are parameterized as below:

$$251 \quad RH_0 = RH - 40 \quad (5)$$

$$252 \quad LR = LR_{dry} \times (0.92 + 2.5 \times 10^{-2}RH_0 - 1.3 \times 10^{-4}RH_0^2 + 2.2 \times 10^{-5}RH_0^3) \quad (6).$$

253 This parameterization equation can be used as a representation of the mean effect of continental
 254 aerosol hygroscopicity on LR.

255 The increase of LR with RH has been studied before. Ackermann (1998) calculated the
 256 relationships of LR with RH by using the lognormal distribution of aerosols as the input of Mie
 257 scattering theory and finds that the LR increases with RH for continental aerosols. However,
 258 Ackermann (1998) shows that the LR doesn't show the same properties for maritime aerosols and
 259 desert aerosols.

260 We theoretically analyze the reasons for the behavior of LR by using the Mie scattering model and
 261 the mean aerosol PNSD of the Hachi campaign. By definition, LR is the ratio of σ_{ext} to β_{sca} . β_{sca} can be
 262 written as $\beta_{sca} = \frac{\sigma_{ext} \times SSA \times PF(180)}{4 \times \pi}$, where the SSA is single scattering albedo, which is defined as the
 263 ratio of extinction coefficient and scattering coefficient; PF(180) is the aerosol scattering phase
 264 function at the scattering angle of 180° . Thus, $LR = \frac{\sigma_{ext} \times 4 \times \pi}{\sigma_{ext} \times SSA \times PF(180)} = \frac{4 \times \pi}{SSA \times PF(180)}$. We use the mean

265 aerosol PNSD as the input of Mie scattering model and calculate the aerosol phase function and SSA
266 values at different RH. When particle grows, there tends to be larger partition of forward scattering and
267 PF(180) is smaller, which is shown in fig.S2. The PF(180) decreases by 40% from 0.27 to 0.16. At the
268 same time, the SSA increases 5% from 0.93 to 0.97 and PF(180) as shown in fig.S3. Thus, the LR
269 increases with the increase of RH.

270 **4.1.2 LR ratio profiles**

271 Four different types of RH profiles and LR profiles are shown in fig 1. In Fig. 1(a), RH values
272 increase with height in the mixed layer and decrease with height above the mixed layer. This is a
273 synthetic result of temperature and water content distributions in the vertical direction. In the summer
274 afternoon, water vapor is well mixed within the mixed layer and decreases sharply above it. P60-70
275 can represent the relatively dry environmental conditions. Statistical results show that P80-90 is most
276 likely to be observed in the environment. P90-95 is a very moist environment condition and its
277 frequency of being observed is second to that of the P80-90 type.

278 Profiles of LR corresponding to RH profiles of the left column are shown in Fig. 1(b). For each
279 type of LR profile, LR increases with height in the mixed layer due to the increase of RH. At the
280 ground, the mean values of LR for each RH profiles are 38.19, 38.28, 39.53 and 40.33 sr, with a
281 standard deviation of 6.20, 6.22, 6.42 and 6.45 respectively. LR changes little from 38 sr at the ground
282 to 42 sr at the top of the mixed layer when the ambient RH is low for the RH profile of P60-70.
283 However, LR grows with a mean value from 40 sr to 60 sr with a relative difference of 50% when the
284 RH is high for the RH profile of P90-95. With such high variation of LR with RH, the retrieved σ_{ext}
285 profiles might be very different when using a constant LR profile instead of a variable one.

286 The black dotted line in Fig. 1(b) is one of the constant column-related LR profiles that are used as
287 an input to retrieve σ_{ext} profiles related to the RH profile P70-80. The constant LR has a higher value at
288 the ground and a lower value at the top of the mixed layer when compared with the calculated variable
289 LR profiles.

290 During the Hachi Campaign, LR values that are calculated by using Mie theory can change from
291 30 to 55 sr within 12 hours at the ground (about 87% of initial value). With high variation of LR over
292 time, the LR profile should be updated in time to get an accurately retrieved σ_{ext} profile. Using only
293 one measurement of LR profile to retrieve the σ_{ext} profiles may lead to great bias of retrieved results
294 (Rosati et al., 2016).

295 **4.2 Bias of retrieved σ_{ext} profiles**

296 With the parameterized σ_{ext} profiles by using the method of section 3.2, we can theoretically get
297 the AOD and the elastic-backscatter lidar signals. Then the AOD and the elastic-backscatter lidar
298 signals can be used to constrain a column-related constant LR profile and to retrieve σ_{ext} profiles.
299 Finally, the retrieved σ_{ext} profiles are compared with the parameterized σ_{ext} profiles and the differences
300 are statistically studied.

301 **4.2.1 Retrieved σ_{ext} profiles vs. original σ_{ext} profiles**

302 Fig. 4 provides an example of the retrieved σ_{ext} profile by using the variable LR profile method
303 and that by using the constant LR profile method from simulated lidar signals. These two kinds of
304 profiles can also be described as a given parameterized σ_{ext} profile and a retrieved σ_{ext} profile from
305 constant LR profile. In Fig. 4(a), the retrieved σ_{ext} profile by using a variable LR profile method is
306 demonstrated by solid line. The dotted line shows the retrieved σ_{ext} profile by using a constant column
307 related LR method. Fig. 4(b) shows the relative bias of the two retrieved σ_{ext} profiles at each height.
308 Fig. 4(c) and (d) are almost the same as Fig. 4(a) and (b) respectively, except that the results of Fig. 4(a)
309 and (b) come from the RH profile of P70-80 while those of Fig. 4(c) and (d) come from the RH profile
310 of P90-95.

311 It is shown in Fig. 4(a) that the retrieved σ_{ext} by using a variable LR profile method increases with
312 height at a rate of $92.25 \text{ (Mm}^{-1}\text{km}^{-1})$ in the mixed layer, which is consistent with the aerosol loading
313 and RH distribution. However, the retrieved σ_{ext} profile by using a constant LR profile method behaves
314 differently and decreases at a rate of $-152.87 \text{ (Mm}^{-1}\text{km}^{-1})$. The structure of σ_{ext} profiles is different by
315 using two different methods. Moreover, the retrieved σ_{ext} from RH profile of P90-95 at the top of the
316 mixed layer is significantly deviated with a relative bias of 40%.

317 Both Fig. 4(a) and (c) show that the retrieved σ_{ext} is overestimated at the ground and
318 underestimated at the top of the mixed layer. From Fig 3(b), it can be concluded that the
319 AOD-constrained constant LR is larger than the calculated true LR at the ground and smaller at the top
320 of the mixed layer. According to formula (3), signals of the elastic-backscatter lidar received at any
321 height are proportional to the backscattering capability of the aerosols. When LR is larger, a larger
322 fraction of the signals transfer forward and less is scattered back. In order to receive the same amount
323 of signal, the backscattering coefficient should be larger and this can lead to the result of a larger σ_{ext} at
324 that layer. Thus, the σ_{ext} tends to be biased higher than the given parameterized σ_{ext} when the LR is

325 larger, and vice versa. Overall, the profiles retrieved by using an AOD-constrained LR can lead to a
326 positive bias at the ground and a negative bias at the top of mixed layer.

327 **4.2.2 Sensitivity Study**

328 Simulations are conducted to study the characteristics of the retrieved σ_{ext} profile bias between
329 using the constant column-related LR profile and variable LR profile. Different kinds of aerosol PNSD,
330 AOD, aerosol hygroscopicity and RH profiles are used. Aerosol PNSD data comes from the Hachi
331 Campaign field measurement. The sensitivity of the bias in aerosol hygroscopicity is evaluated by
332 changing the size-resolved κ value. Aerosols are defined to have high hygroscopicity when the aerosol
333 size-resolved κ value is one standard deviation above the mean of the size-resolved κ value. They are
334 defined as low hygroscopicity if the size-resolved κ value is one standard deviation below mean of the
335 size-resolved κ value. Four different kinds of RH profiles are also used in this sensitivity study. As
336 discussed in section 3.2.1, a negative bias at the top of the mixed layer is accompanied by a positive
337 bias at the ground and the largest bias happens at the top of the mixed layer. It is sufficient to focus on
338 the relative bias at the top of the mixed layer.

339 Statistical characteristics of the relative bias at the top of the mixed layer are shown in Fig. 5.
340 Different panels represent the results of different aerosol hygroscopicity. The left column shows the
341 results of low aerosol hygroscopicity. Middle panel shows results from mean aerosol hygroscopicity.
342 High aerosol hygroscopicity of particles results in the properties shown in the right panel. For each
343 panel, relationships between relative bias and AOD are shown. Different colors in each panel show the
344 results of different RH profiles. Filled colors represent the ranges of the relative bias at one standard
345 deviation of using different PNSD.

346 Every panel shows that relative bias clearly increases with the enhancement of RH in the
347 surroundings. The relative bias has a mean value of less than 10% for the RH profile of P60-70. LR
348 has little variation when the surrounding RH is low and the bias has a low value. For RH profiles of
349 P70-80 and P80-90, the relative bias increases with RH and increases strongly up to 25% when the
350 surrounding relative humidity is high. These behaviors of relative difference under difference RH
351 conditions are consistent with the change of LR with RH.

352 Filled color ranges of relative bias at given AOD and RH profile result from the variation of
353 aerosol PNSD. The LR enhancement factor can have different behavior with different aerosol PNSD
354 according to Mie scattering theory. Changing the aerosol PNSD leads to a wider range of bias when

355 the RH is higher. Fig. 5 also shows that different PNSD can change the relative bias by a mean value
356 of 10% for different polluted conditions.

357 Relative bias increases with AOD value when the AOD is low, while it remains constant when the
358 AOD is high. When AOD is low, the amount of scattered light by air molecules occupies a large
359 fraction. Air molecules have a constant LR of $\frac{8}{3}\pi$ sr according the Rayleigh scattering theory. The
360 relative bias of retrieved σ_{ext} profile is relatively small when the AOD is low. When the AOD has a
361 larger value, backscattered signals mainly depend on aerosol backscattering and the signals
362 backscattered by air molecules are negligible. Relative bias mainly reflects the impacts of aerosol
363 hygroscopicity. The mean relative bias increases from 26% to 32% at high RH conditions with the
364 increase of aerosol hygroscopicity. Aerosol hygroscopicity should be taken into account under high
365 RH conditions.

366 To sum up, RH is one of the most important factors that influence the accuracy of retrieving the
367 elastic-backscatter lidar data. Different PNSD can also lead to a large variation of relative difference.
368 The relative difference increases with the AOD when the AOD is low, but increases little when the
369 AOD is high. Under the conditions of both high values of RH and AOD, the relative bias of retrieved
370 data reaches a maximum due to the influence of aerosol hygroscopic growth.

371 **4.3 Evaluation of LR enhancement factor parameterization**

372 Simulations are carried out to test the accuracy of the new methods of retrieving the σ_{ext} profiles,
373 which is proposed in section 3.4.2. These simulations employ the elastic-backscattering lidar signals
374 from section 3.3, the RH profiles, the integrated AOD values of the parameterized σ_{ext} profiles and the
375 parameterization scheme of LR enhancement factor formulas (5), (6). With this information, the σ_{ext}
376 profiles are retrieved by the method of section 3.4.2. We then studied the relative biases between the
377 parameterized σ_{ext} profiles and the retrieved σ_{ext} profiles by using the new method.

378 Different kinds of aerosol PNSD, AOD, aerosol hygroscopicity and RH profiles are used in the
379 simulations. The relative bias are statistically studied and summarized. The values listed in Table 1 are
380 the mean relative biases under different PNSD conditions. From Table 1, we can see that all of the
381 relative bias is within the range of 13% for different PNSD, AOD, aerosol hygroscopicity and RH
382 profiles. This indicates that the algorithm of using the mean LR enhancement factor parameterization
383 scheme is feasible and can decrease the bias of the retrieved elastic-backscatter lidar data significantly.

384 **4.4 Retrieving the real-time measurement elastic-backscatter lidar signals**

385 MPL data and AERONET data are employed to validate the algorithm of retrieving the
386 elastic-backscatter lidar data on the day of 5 July 2016. After quality control of data processing,
387 elastic-backscatter lidar data is retrieved by using both a constant LR profile method and a
388 parameterized variable LR profile method. Details of retrieving the MPL signals and the auxiliary
389 information are shown in fig.S5. Fig. 6 gives the retrieved σ_{ext} profiles for two of local times: 13:00 (a)
390 and 14:30 (b).

391 Fig. 6(a) is a typical case of the retrieved σ_{ext} profiles under high values of both RH and AOD
392 conditions. The retrieved σ_{ext} profiles by using the constant LR profile method and variable LR profile
393 method show almost the same properties as the simulations. The relative bias reaches a value of 39.3%
394 at an altitude of 1.57 km. These differences of retrieved σ_{ext} profiles may lead to a significant bias of
395 estimating the mixed layer height and have significant impact on radiative energy distribution in the
396 vertical direction. Fig. 6(b) shows the retrieved σ_{ext} profiles of different structures from the same
397 elastic-backscatter lidar data. The retrieved σ_{ext} by using variable LR profile method increases with
398 height within the mixed layer. However, the retrieved σ_{ext} by using constant LR profile decreases
399 slightly with height within the mixed layer.

400 **5 Conclusions**

401 The influence of aerosol hygroscopic growth on LR is evaluated by using Mie scattering theory.
402 Datasets used as input to Mie theory model come from the Hachi Campaign field measurements and
403 these datasets can be used as a good representation of the continental aerosols. Results show that LR in
404 the NCP mainly ranges from 30 to 90 sr, which is consistent with literature values of continental
405 aerosols. LR could be enhanced significantly under high RH conditions, with a mean factor of 2.2 at
406 92% RH.

407 RH in the mixed layer in the NCP is frequently observed to be higher than 90%. Under these
408 conditions, a large variation of LR in the vertical direction exists. This leads to significant bias of
409 retrieved σ_{ext} profile due to a constant LR profile currently used to retrieve the elastic-backscatter lidar
410 signals. The relative bias of the retrieved σ_{ext} profiles between the constant LR profile method and the
411 variable LR profile method can reach up to 40% under high RH conditions.

412 Sensitivity studies were carried out to test the bias of retrieved σ_{ext} profiles. The bias increased
413 linearly with RH at low RH but increased strongly at high RH. Different PNSDs can lead to 10%

414 standard deviation of the bias. Maximum bias happens under the conditions of both high AOD and RH
415 that frequently happen in the NCP. The influence of aerosol hygroscopic growth on LR should be
416 taken into consideration when retrieving the elastic-backscatter lidar data in the NCP.

417 A new algorithm accounting for the aerosol hygroscopic growth is proposed to retrieve the
418 elastic-backscatter lidar data. A scheme of LR enhancement factor parameterization is introduced in
419 this algorithm. The bias of retrieved σ_{ext} profiles by using this algorithm can be constrained within
420 13%. Real-time measurement of MPL data is employed to validate the algorithm and the results show
421 good consistency with the simulations.

422 This research will advance our understanding of the influence of aerosol hygroscopic growth on
423 LR and help to improve the retrieval of σ_{ext} profile from elastic-backscatter lidar signals.

424

425 **Acknowledgments**

426 This work is supported by the National Natural Science Foundation of China (41590872,
427 41375134).

428

429

430 **References**

- 431 Ackermann, J. (1998) The Extinction-to-Backscatter Ratio of Tropospheric Aerosol: A Numerical Study. *Journal of*
432 *Atmospheric and Oceanic Technology* 15, 1043-1050.
- 433 Anderson, T.L., Anderson, T.L. (2003) Variability of aerosol optical properties derived from in situ aircraft measurements
434 during ACE-Asia. *Journal of Geophysical Research* 108, ACE-15-11-ACE 15-19.
- 435 Anderson, T.L., Masonis, S.J., Covert, D.S., Charlson, R.J., Rood, M.J. (2000) In situ measurement of the aerosol
436 extinction-to-backscatter ratio at a polluted continental site. *Journal of Geophysical Research: Atmospheres* 105,
437 26907-26915.
- 438 Andreae, M.O., Crutzen, P.J. (1997) Atmospheric Aerosols: Biogeochemical Sources and Role in Atmospheric Chemistry.
439 *Science* 276, 1052-1058.
- 440 Ansmann, A., Wagner, F., Althausen, D., Müller, D., Herber, A., Wandinger, U. (2001) European pollution outbreaks during
441 ACE 2: Lofted aerosol plumes observed with Raman lidar at the Portuguese coast. *Journal of Geophysical Research*
442 *Atmospheres* 106, 20725–20733.
- 443 Ansmann, A., Wagner, F., Müller, D., Althausen, D., Herber, A., von Hoyningen-Huene, W., Wandinger, U. (2002) European
444 pollution outbreaks during ACE 2: Optical particle properties inferred from multiwavelength lidar and star-Sun photometry.
445 *Journal of Geophysical Research: Atmospheres* 107, AAC 8-1-AAC 8-14.
- 446 Bian, J., Chen, H., ouml, mel, H., Duan, Y. (2011) Intercomparison of humidity and temperature sensors: GTS1, Vaisala RS80,
447 and CFH. *Advances in atmospheric sciences* 28, 139-146.
- 448 Bohren, C.F., Huffman, D.R., (2007) Absorption and Scattering by an Arbitrary Particle, *Absorption and Scattering of Light*

449 by Small Particles. Wiley-VCH Verlag GmbH, pp. 57-81.

450 Chaikovskiy, A., Dubovik, O., Holben, B., Bril, A., Goloub, P., Tanre, D., Pappalardo, G., Wandinger, U., Chaikovskaya, L.,
451 Denisov, S., Grudo, J., Lopatin, A., Karol, Y., Lapyonok, T., Amiridis, V., Ansmann, A., Apituley, A., Allados-Arboledas, L.,
452 Biniotoglou, I., Boselli, A., D'Amico, G., Freudenthaler, V., Giles, D., Jose Granados-Munoz, M., Kokkalis, P., Nicolae, D.,
453 Oshchepkov, S., Papayannis, A., Perrone, M.R., Pietruczuk, A., Rocadenbosch, F., Sicard, M., Slutsker, I., Talianu, C., De
454 Tomasi, F., Tsekeri, A., Wagner, J., Wang, X. (2016) Lidar-Radiometer Inversion Code (LIRIC) for the retrieval of vertical
455 aerosol properties from combined lidar/radiometer data: development and distribution in EARLINET. *Atmospheric*
456 *Measurement Techniques* 9, 1181-1205.

457 Chen, J., Zhao, C.S., Ma, N., Liu, P.F., Göbel, T., Hallbauer, E., Deng, Z.Z., Ran, L., Xu, W.Y., Liang, Z., Liu, H.J., Yan, P., Zhou,
458 X.J., Wiedensohler, A. (2012) A parameterization of low visibilities for hazy days in the North China Plain. *Atmos. Chem.*
459 *Phys.* 12, 4935-4950.

460 Chen, J., Zhao, C.S., Ma, N., Yan, P. (2014) Aerosol hygroscopicity parameter derived from the light scattering enhancement
461 factor measurements in the North China Plain. *Atmos. Chem. Phys.* 14, 8105-8118.

462 Fernald, F.G. (1984) Analysis of atmospheric lidar observations: some comments. *Applied Optics* 23, 652-653.

463 Fernald, F.G., Herman, B.M., Reagan, J.A. (1972) Determination of Aerosol Height Distributions by Lidar. *Journal of Applied*
464 *Meteorology* 11, 482-489.

465 Ferrare, R.A., Melfi, S.H., Whiteman, D.N., Evans, K.D., Poellot, M., Kaufman, Y.J. (1998) Raman lidar measurements of
466 aerosol extinction and backscattering: 2. Derivation of aerosol real refractive index, single-scattering albedo, and
467 humidification factor using Raman lidar and aircraft size distribution measurements. *Journal of Geophysical Research:*
468 *Atmospheres* 103, 19673-19689.

469 Ferrare, R.A., Turner, D.D., Brasseur, L.H., Feltz, W.F., Dubovik, O., Tooman, T.P. (2001) Raman lidar measurements of the
470 aerosol extinction-to-backscatter ratio over the Southern Great Plains. *Journal of Geophysical Research: Atmospheres* 106,
471 20333-20347.

472 Ferrero, L., Mocnik, G., Ferrini, B.S., Perrone, M.G., Sangiorgi, G., Bolzacchini, E. (2011) Vertical profiles of aerosol
473 absorption coefficient from micro-Aethalometer data and Mie calculation over Milan. *Science of the Total Environment*
474 409, 2824-2837.

475 Ferrero, L., Perrone, M.G., Petraccone, S., Sangiorgi, G., Ferrini, B.S., Lo Porto, C., Lazzati, Z., Cocchi, D., Bruno, F., Greco, F.,
476 Riccio, A., Bolzacchini, E. (2010) Vertically-resolved particle size distribution within and above the mixing layer over the
477 Milan metropolitan area. *Atmospheric Chemistry and Physics* 10, 3915-3932.

478 Gasteiger, J., Groß, S., Sauer, D., Haarig, M., Ansmann, A., Weinzierl, B. (2017) Particle settling and vertical mixing in the
479 Saharan Air Layer as seen from an integrated model, lidar, and in situ perspective. *Atmospheric Chemistry and Physics* 17,
480 297-311.

481 He, Q.S., Li, C.C., Mao, J.T., Lau, A.K.H., Li, P.R. (2006) A study on the aerosol extinction-to-backscatter ratio with
482 combination of micro-pulse LIDAR and MODIS over Hong Kong. *Atmospheric Chemistry and Physics* 6, 3243-3256.

483 Klett, J.D. (1981) Stable analytical inversion solution for processing lidar returns. *Applied Optics* 20, 211-220.

484 Klett, J.D. (1985) Lidar inversion with variable backscatter/extinction ratios. *Applied Optics* 24, 1638-1643.

485 Kuang, Y., Zhao, C.S., Tao, J.C., Bian, Y.X., Ma, N. (2016) Impact of aerosol hygroscopic growth on the direct aerosol
486 radiative effect in summer on North China Plain. *Atmospheric Environment* 147, 224-233.

487 Kuang, Y., Zhao, C.S., Tao, J.C., Ma, N. (2015) Diurnal variations of aerosol optical properties in the North China Plain and
488 their influences on the estimates of direct aerosol radiative effect. *Atmos. Chem. Phys.* 15, 5761-5772.

489 Liu, H.J., Zhao, C.S., Nekat, B., Ma, N., Wiedensohler, A., van Pinxteren, D., Spindler, G., Müller, K., Herrmann, H. (2014)
490 Aerosol hygroscopicity derived from size-segregated chemical composition and its parameterization in the North China
491 Plain. *Atmospheric Chemistry and Physics* 14, 2525-2539.

492 Liu, P., Zhao, C., Zhang, Q., Deng, Z., Huang, M., Xincheng, M.A., Tie, X. (2009) Aircraft study of aerosol vertical

493 distributions over Beijing and their optical properties. *Tellus Series B-Chemical & Physical Meteorology* 61, 756–767.

494 Liu, P.F., Zhao, C.S., Göbel, T., Hallbauer, E., Nowak, A., Ran, L., Xu, W.Y., Deng, Z.Z., Ma, N., Mildenerger, K., Henning, S.,

495 Stratmann, F., Wiedensohler, A. (2011) Hygroscopic properties of aerosol particles at high relative humidity and their

496 diurnal variations in the North China Plain. *Atmos. Chem. Phys.* 11, 3479-3494.

497 Ma, N., Zhao, C.S., Müller, T., Cheng, Y.F., Liu, P.F., Deng, Z.Z., Xu, W.Y., Ran, L., Nekat, B., van Pinxteren, D., Gnauk, T., Müller,

498 K., Herrmann, H., Yan, P., Zhou, X.J., Wiedensohler, A. (2012) A new method to determine the mixing state of light

499 absorbing carbonaceous using the measured aerosol optical properties and number size distributions. *Atmos. Chem. Phys.*

500 12, 2381-2397.

501 Ma, N., Zhao, C.S., Nowak, A., Müller, T., Pfeifer, S., Cheng, Y.F., Deng, Z.Z., Liu, P.F., Xu, W.Y., Ran, L., Yan, P., Göbel, T.,

502 Hallbauer, E., Mildenerger, K., Henning, S., Yu, J., Chen, L.L., Zhou, X.J., Stratmann, F., Wiedensohler, A. (2011) Aerosol

503 optical properties in the North China Plain during HaChi campaign: an in-situ optical closure study. *Atmos. Chem. Phys.* 11,

504 5959-5973.

505 Pappalardo, G., Amodeo, A., Mona, L., Pandolfi, M., Pergola, N., Cuomo, V. (2004a) Raman lidar observations of aerosol

506 emitted during the 2002 Etna eruption. *Geophysical Research Letters* 31, 179-211.

507 Pappalardo, G., Amodeo, A., Pandolfi, M., Wandinger, U., Ansmann, A., Bösenberg, J., Matthias, V., Amiridis, V., De Tomasi,

508 F., Frioud, M., Iarlori, M., Komguem, L., Papayannis, A., Rocadenbosch, F., Wang, X. (2004b) Aerosol lidar intercomparison

509 in the framework of the EARLINET project. 3. Ramanlidar algorithm for aerosol extinction, backscatter, and lidar ratio.

510 *Applied Optics* 43, 5370-5385.

511 Petters, M.D., Kreidenweis, S.M. (2007) A single parameter representation of hygroscopic growth and cloud condensation

512 nucleus activity. *Atmos. Chem. Phys.* 7, 1961-1971.

513 Pietruczuk, A., Podgórski, J., (2009) The lidar ratio derived from sun-photometer measurements at Belsk Geophysical

514 Observatory, *Acta Geophysica*, p. 476.

515 Pietruczuk, A., Podgorski, J. (2009) The lidar ratio derived from sun-photometer measurements at Belsk Geophysical

516 Observatory. *Acta Geophysica* 57, 476-493.

517 Ran, L., Deng, Z., Xu, X., Yan, P., Lin, W., Wang, Y., Tian, P., Wang, P., Pan, W., Lu, D. (2016) Vertical profiles of black carbon

518 measured by a micro-aethalometer in summer in the North China Plain. *Atmospheric Chemistry and Physics* 16,

519 10441-10454.

520 Rosati, B., Herrmann, E., Bucci, S., Fierli, F., Cairo, F., Gysel, M., Tillmann, R., Größ, J., Gobbi, G.P., Di Liberto, L.,

521 Di Donfrancesco, G., Wiedensohler, A., Weingartner, E., Virtanen, A., Mentel, T.F., Baltensperger, U. (2016) Studying the

522 vertical aerosol extinction coefficient by comparing in situ airborne data and elastic backscatter lidar. *Atmospheric*

523 *Chemistry and Physics* 16, 4539-4554.

524 She, C.Y., Alvarez, R.J., Caldwell, L.M., Krueger, D.A. (1992) High-spectral-resolution Rayleigh–Mie lidar measurement

525 of aerosol and atmospheric profiles. *Optics Letters* 17, 541-543.

526 Shipley, S.T., Tracy, D.H., Eloranta, E.W., Trauger, J.T., Sroga, J.T., Roesler, F.L., Weinman, J.A. (1983) High spectral resolution

527 lidar to measure optical scattering properties of atmospheric aerosols. 1: Theory and instrumentation. *Applied Optics* 22,

528 3716-3724.

529 Sroga, J.T., Eloranta, E.W., Shipley, S.T., Roesler, F.L., Tryon, P.J. (1983) High spectral resolution lidar to measure optical

530 scattering properties of atmospheric aerosols. 2: Calibration and data analysis. *Applied Optics* 22, 3725-3732.

531 Sušnik, A., Holder, H., Eichinger, W. (2014) A Minimum Variance Method for Lidar Signal Inversion. *Journal of Atmospheric*

532 *and Oceanic Technology* 31, 468-473.

533 Wex, H., Neususs, C., Wendisch, M., Stratmann, F., Koziar, C., Keil, A., Wiedensohler, A., Ebert, M. (2002) Particle scattering,

534 backscattering, and absorption coefficients: An in situ closure and sensitivity study. *Journal Of Geophysical*

535 *Research-Atmospheres* 107.

536 Xu, W.Y., Zhao, C.S., Ran, L., Deng, Z.Z., Liu, P.F., Ma, N., Lin, W.L., Xu, X.B., Yan, P., He, X., Yu, J., Liang, W.D., Chen, L.L. (2011)

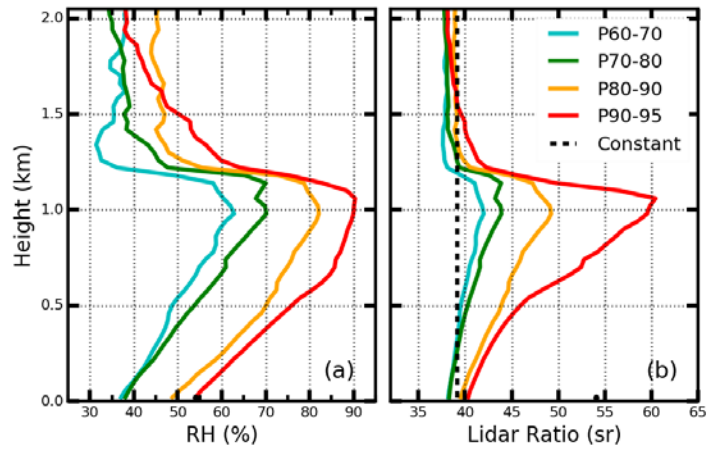
537 Characteristics of pollutants and their correlation to meteorological conditions at a suburban site in the North China Plain.
538 Atmos. Chem. Phys. 11, 4353-4369.
539
540

541 **Table 1.** Relative difference (%) between the σ_{ext} profiles by using the proposed new method and the parameterized σ_{ext}
 542 profiles under different AOD and RH profile conditions

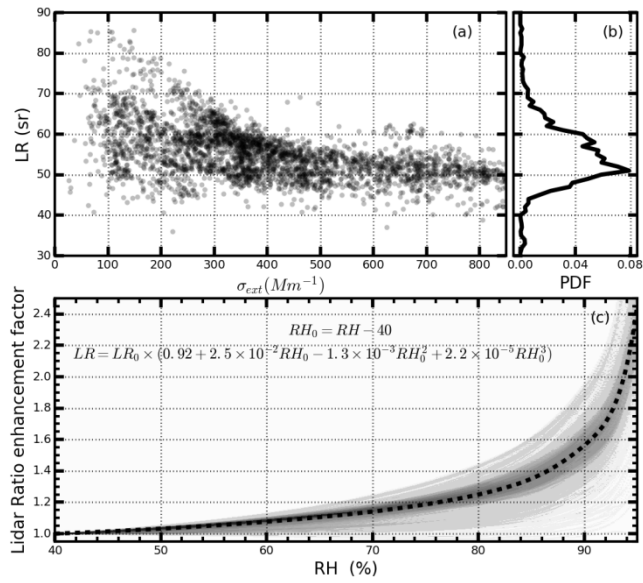
		AOD							
		0.2	0.4	0.6	0.8	1.0	1.2	1.4	1.6
RH profile	P60-70	6	9	11	13	8	8	8	9
	P70-80	7	7	9	12	7	6	7	8
	P80-90	8	5	4	11	6	5	5	6
	P90-95	9	6	6	9	13	7	7	9

543

544



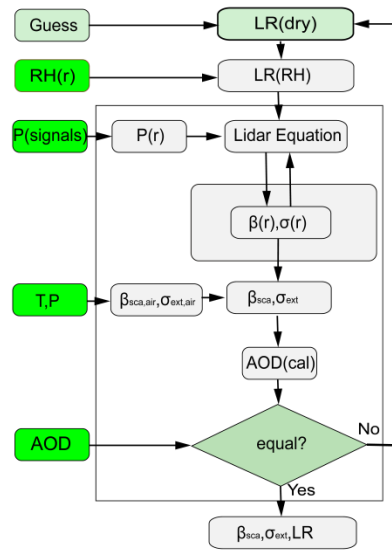
545
 546 **Figure 1.** (a) Four kinds of RH profiles P60-70, P70-80, P80-90, and P90-95; (b) calculated LR profiles from the
 547 corresponding RH profiles of (a). The dotted black line is one of the constant LR profiles that are used to retrieve the
 548 MPL signals.
 549



550
 551 **Figure 2.** LR distribution and LR enhancement factor during the Hachi campaign. (a) LR distribution under different
 552 polluted conditions. (b) Probability distribution of the LR. (c) Enhancement factor of the LR. Dotted line is the mean
 553 fit LR enhancement factor.
 554
 555

556

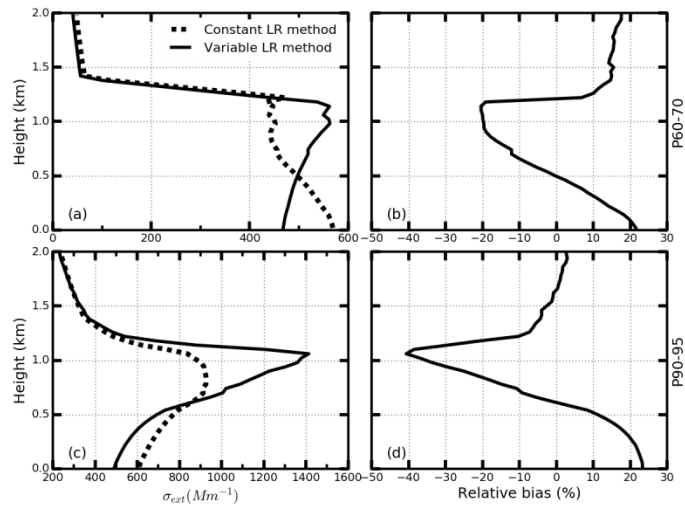
557



558

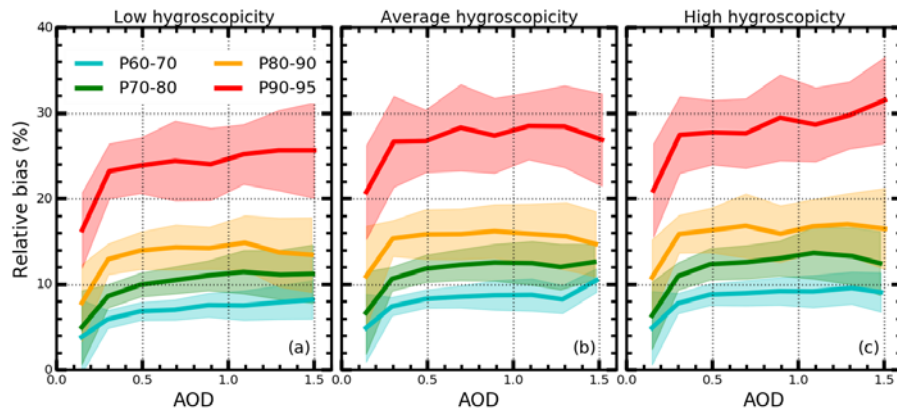
559 **Figure 3.** Schematic diagram of retrieving the σ_{ext} profile. The input variables are displayed in a green background.

560

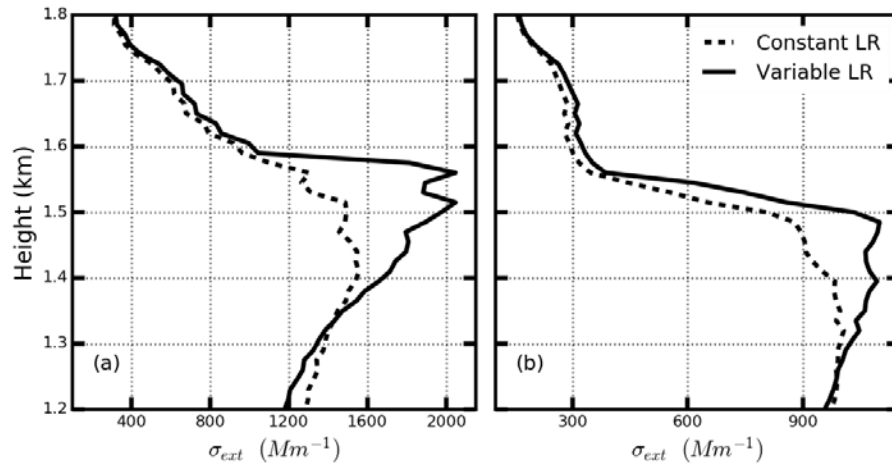


562

563 **Figure 4.** (a) Retrieved σ_{aero} profiles using constant LR profile method (dotted line) and variable LR profile method
 564 (solid line) from simulated lidar signals. (b) The relative bias of the retrieved σ_{aero} profile using two different methods.
 565 (c),(d) are the same as (a), (b) respectively. The LR signals of panel (a) results form P70-80 RH profile, and LR
 566 signals of panel (b) results from P90-95 RH profile.



567
 568 **Figure 5.** Relative bias of the retrieved σ_{ext} under different AOD, PNSD, and hygroscopicity and RH profiles
 569 conditions. Different colors represent different RH profile. Panel (a) is derived from the low hygroscopicity. Panel (b)
 570 results from the mean hygroscopicity. Panel (c) is for high hygroscopicity.



571
 572 **Figure 6.** Retrieved σ_{ext} profiles from field measurement MPL signals at (a) 13:00 and (b) 14:30 on July 5, 2016. The
 573 dotted line represents the retrieved σ_{ext} profiles using constant LR profile method. The solid line represents the retrieved σ_{ext}
 574 profiles using the variable LR profile method.